

Renormalization-Inspired Effective Field Neural Networks for Scalable Modeling of Classical and Quantum Many-Body Systems

Xi Liu,¹ Yujun Zhao,¹ Chun Yu Wan,¹ Yang Zhang,^{2,3} and Junwei Liu^{1,*}

¹*Department of Physics, Hong Kong University of Science and Technology, Clear Water Bay, Hong Kong SAR, China*

²*Department of Physics and Astronomy, University of Tennessee, Knoxville, TN 37996, USA*

³*Min H. Kao Department of Electrical Engineering and Computer Science, University of Tennessee, Knoxville, Tennessee 37996, USA*

(Dated: March 19, 2026)

We introduce Effective Field Neural Networks (EFNNs), a new architecture based on continued functions—mathematical tools used in renormalization to handle divergent perturbative series. Our key insight is that neural networks can implement these continued functions directly, providing a principled approach to many-body interactions. Testing on three systems (a classical 3-spin infinite-range model, a continuous classical Heisenberg spin system, and a quantum double exchange model), we find that EFNN outperforms standard deep networks, ResNet, and DenseNet. Most striking is EFNN’s generalization: trained on 10×10 lattices, it accurately predicts behavior on systems up to 40×40 with no additional training—and the accuracy improves with system size, with a computational time speed-up of 10^3 compared to ED for 40×40 lattice. This demonstrates that EFNN captures the underlying physics rather than merely fitting data, making it valuable beyond many-body problems to any field where renormalization ideas apply.

The collective behaviors of many interacting particles—such as spins, molecules, and atoms—give rise to some of the most intriguing phenomena in condensed matter physics. However, theoretical and computational studies of many-body problems often confront the curse of dimensionality and one must devise strategies to circumvent it. Machine learning has emerged as a powerful tool for extracting effective features from high-dimensional datasets and tackling long-standing problems in condensed matter physics. Numerous machine learning techniques have been applied to a wide range of classical and quantum many-body systems, including classifying phases of matter with supervised [1–3] and unsupervised machine learning [4–8], representing many-body quantum states [9–13], accelerating Monte Carlo simulations [14–17], fitting high-dimensional potential energy surfaces [18–22] and searching for spin glass ground states [23].

Standard deep neural networks (DNNs) are ineffective in solving many-body problems unless augmented with physical knowledge. For example, an 8×8 classical two-dimensional Ising model requires highly complex DNN structures [24]. Consequently, extensive research has focused on encoding physics into neural network architectures to enhance their effectiveness in physical applications, including incorporating physical laws and constraints [25–40]. These physics-encoded neural networks have found applications in computing effective Hamiltonians [41–43], property prediction [36, 39, 41, 43–49], structure search [37, 38], etc. These methods, although often outperforming standard DNNs, tend to rely on intuitive and simplified imitations of physical principles, and still remain elusive in revealing the underlying many-body interactions.

In this work, we propose Effective Field Neural Networks (EFNNs), a new architecture inspired by field theory. The core motivation is to decompose many-body interactions into single quasi-particle representations governed by an emergent effective field. Unlike standard DNNs where adjacent layers rely only on previous layers, EFNNs incorporate initial features at every layer, forming a self-similar structure trained via recursive self-refining that captures many-body interactions through renormalization principles. Unlike approaches such as FermiNet [50], which directly parameterizes high-dimensional wave-functions without explicit separation of quasi-particles and fields, our method does not presuppose a fixed ansatz for the wavefunction. Instead, the quasi-particle and effective field representations are learned through a recursive self-refining process, mirroring the renormalization group (RG) framework in field theory, while leveraging the expressive power of deep neural networks. This recursive approach progressively refines the accuracy of both the quasi-particle and effective field descriptions.

We first illustrate the EFNN architecture by reformulating the classical 2D Ising model within the EFNN framework. The Hamiltonian of a classical 2D Ising model is defined as $H(S) = -J \sum_{\langle i,j \rangle} s_i s_j$, where $\langle i,j \rangle$ denotes a summation over pairs of nearest-neighbor sites, $s_i = \pm 1$ represents the spin at site i , J is the interaction strength between two spins, and S is the collection of all spins. We define the effective field on spin s_i as $\phi_i(S) = -\frac{J}{2} \times (\text{sum of nearest neighbors})$, and the quasi-particle as $s_i \phi_i(S)$, yielding total energy $H(S) = \sum_i s_i \phi_i(S)$. As illustrated schematically in Fig. 1(a), the interacting spins are first mapped to an effective field, then the effective field element-wise multiplied with the interacting spins is mapped to independent spins. Finally, a summation is performed over the independent spins, and the total energy is obtained. We reformulate this as a neural

* liuj@ust.hk

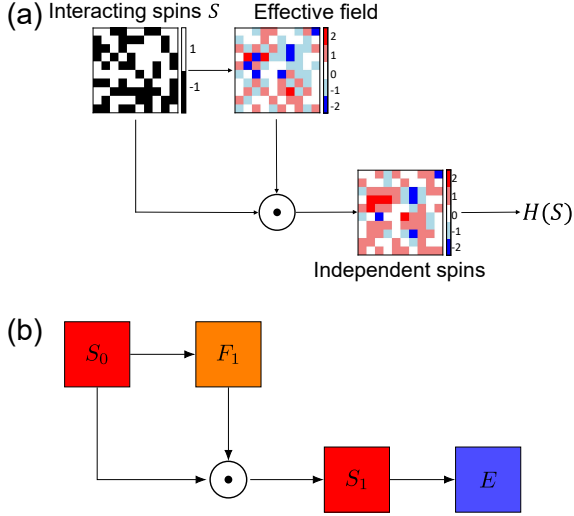


FIG. 1. Energy evaluation of a 2D Ising model reformulated as a neural network. (a) Calculation of the effective field by summing the interacting spins. Each interacting spin is multiplied by its corresponding effective field to obtain independent spin values, and the total energy is determined by summing up these independent spins. (b) Neural network representation of the energy evaluation process. \odot represents the element-wise multiplication.

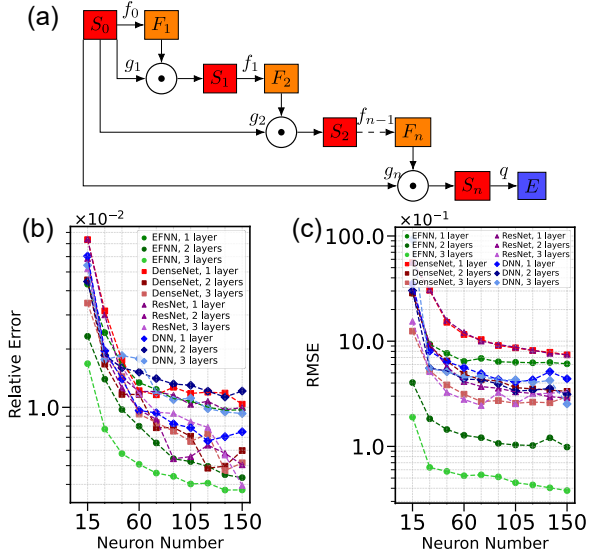


FIG. 2. Performance of EFNNs on a classical 3-spin infinite range model and classical Heisenberg spin system. (a) Architecture of the EFNN. (b) Performance of EFNNs, DenseNets, ResNets, DNNs on 3-spin infinite range model. (c) Performance of EFNNs, DenseNets, ResNets, DNNs on classical Heisenberg spin system.

network structure (Fig. 1(b)), where $S_0 = S$ represents the interacting spins. The effective field layer F_1 and the quasi-particle layer S_1 constitute a single field-particle (FP) layer. The evaluation of S_1 relies on both the effec-

tive layer F_1 and the interacting spin layer S_0 , therefore a connection is required from S_0 to S_1 , as well as from F_1 to S_1 , distinguishing this architecture from a standard DNN. Finally, a summation is performed over S_1 to obtain the energy E .

In the classical 2D Ising model, both the effective field and quasi-particles can be exactly calculated, which, however, becomes infeasible for more complicated many-body interactions. Following the spirit of renormalization from field theory, we can recursively refine the evaluations of the effective field and the quasi-particles. This recursive structure, when combined with the multiplicative interactions and self-similar connectivity pattern, implements a continued function—a mathematical tool from renormalization theory for handling divergent perturbative series (see Supplementary Material [51] for the complete derivation). As shown in Fig. 2(a), we can extend the FP layer number in Fig. 1(b) to obtain the deep Effective Field Neural Networks. The evaluation procedure is detailed as

$$F_i = f_{i-1}(S_{i-1}), S_i = g_i(S_0) \odot F_i, E = q(S_n),$$

where the function f_{i-1} maps the previous quasi-particle layer S_{i-1} (for $i \geq 2$) or the initial layer S_0 (for $i = 1$) to the effective field layer F_i . The input layer S_0 is first processed by g_i , then element-wise multiplied by F_i to produce the quasi-particle layer S_i . Each FP layer consists of F_i and S_i . The final quasi-particle layer S_n generates the output energy E through the function q , which sums all elements of the last layer. The functions f_i are nonlinear (specifically, we use hyperbolic tangent functions) to implement renormalization by ensuring finite values, while g_j are nonlinear to enhance expressiveness. Linear functions may suffice only for simpler models like the classical 2D Ising model with nearest-neighbor interactions.

We present three case studies to demonstrate the capability of EFNNs to capture many-body interactions. The first case study focuses on the classical 3-spin infinite-range model in 1D, with Hamiltonian:

$$H(S) = - \sum_{i < j < k} J_{ijk} s_i s_j s_k, \quad (1)$$

where the spins take binary values $\{0, 1\}$, J_{ijk} are constants, and the system comprises 15 lattice sites. We train EFNNs to evaluate $H(S)$ in Eq. (1), and compare its performance with those of DenseNets, ResNets, and DNNs.

We generate 16000 training and 4000 test samples using Eq. (1). The nonlinear mappings f_i and g_j use sequential linear layers with tanh activations. The network is trained with the Adam optimizer and a decaying learning rate. Performance is evaluated by the relative error, defined as the root mean square error (RMSE) on the test set divided by the absolute value of the mean of $H(S)$. We vary the number of network layers from 1 to 3 and the number of neurons from 15 to 150. The performance of EFNNs, DenseNets, ResNets, and DNNs is

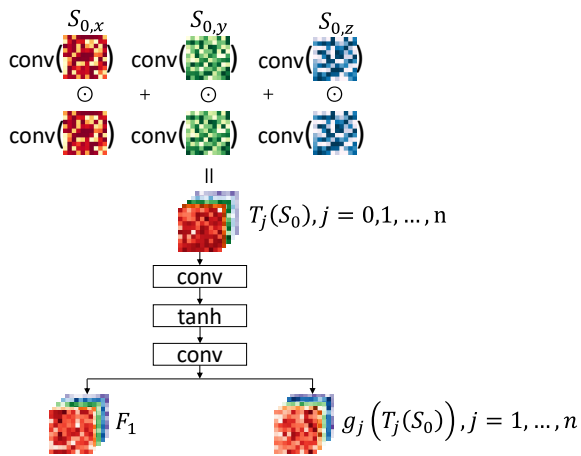


FIG. 3. Symmetrization: Each of the three channels of S_0 ($S_{0,x}$, $S_{0,y}$, $S_{0,z}$) undergoes convolution and element-wise multiplication within the same channel. The resulting products are summed to form the symmetrization layer $T_j(S_0)$. Subsequently, $T_j(S_0)$ is passed through a sequence of layers—convolution, tanh activation, and another convolution

—to produce F_1 for $j = 0$ or $g_j(T_j(S_0))$ for $j = 1, \dots, n$.

presented in Fig. 2(b). The relative error decreases with more neurons for all networks, but EFNNs significantly outperform others as layers increase, with the relative error decreasing below 5×10^{-3} for EFNNs with 2 and 3 layers when the number of neurons ≥ 105 . The only exception is the ResNet with 3 layers and 150 neurons. In most cases, DenseNets, ResNets, and DNNs perform worse than 2-layer EFNNs.

To test the capability of EFNNs beyond discrete systems, our second case study examines a classical Heisenberg spin system, using the same three-body interaction model in Eq. (1) with continuous spins, where s_i takes continuous values in $[-1, 1]$ rather than discrete values 0, 1. We use the RMSE of the total energy as the performance metric, with results shown in Fig. 2(c), since the average value of Eq. (1) is 0. Compared to the discrete case, the configuration space is now continuous, yet EFNNs with 2 and 3 layers still outperform all other networks. Fig. 2(c) also shows the general trend that the error decreases with increasing number of neurons. The most accurate result is achieved by the 3-layer EFNN with 150 neurons, where the error of the total energy reduces to 4×10^{-2} . These results demonstrate that EFNNs effectively capture many-body interactions through the renormalization procedure of their recursive continued-function structure; failing to incorporate this structure leads to inaccurate results. We show in the Supplementary Material [51] that DNNs completely lack the structure of a continued function, while DenseNets and ResNets misrepresent a continued function.

We proceed to our third, more challenging case study: evaluating the Monte Carlo energy of the quantum double exchange model [52–54] at finite temperature. The

Hamiltonian of an $N \times N$ lattice reads

$$H(S) = -t \sum_{\langle i,j \rangle, \alpha} \left(\hat{c}_{i\alpha}^\dagger \hat{c}_{j\alpha} + \text{h.c.} \right) - \frac{J}{2} \sum_{i, \alpha, \beta} \vec{s}_i \cdot \hat{c}_{i\alpha}^\dagger \vec{\sigma}_{\alpha\beta} \hat{c}_{i\beta}, \quad (2)$$

where $\langle i, j \rangle$ denotes nearest neighbors, $\hat{c}_{i\alpha}$ is the electron annihilation operator with spin α at site i , $\vec{\sigma}$ are the Pauli matrices, and $\vec{s}_i \in \mathbb{S}^2$ is a 3D classical unit vector representing the local spin at site i , the classical spin interacts with the electrons through an on-site coupling, and S is the collection of all classical spins \vec{s}_i . We set $N = 10$, $J = 16t$, $\mu = -8.3t$, $T = 0.1t$, $t = 1$.

At finite temperature T , the Monte Carlo energy $E_{\text{MC}}(S) = -T \sum_n \log(1 + e^{-E_n(S)/T})$ determines the acceptance ratio in Monte Carlo simulations, where $E_n(S)$ are the eigenvalues of $H(S)$ with chemical potential in Eq. (2). Computing the exact value of $E_{\text{MC}}(S)$ requires diagonalization of Eq. (2) at each Monte Carlo update step, incurring $O(N^6)$ computational complexity per step. With millions of Monte Carlo steps required for convergence, this approach becomes computationally prohibitive. An intuitive solution is to approximate $E_{\text{MC}}(S)$ using a perturbative expansion, yielding an effective model with RKKY-type interactions [55–57]. This effective model with 2-body interactions has proven sufficiently accurate to replace exact diagonalization in Determinant Quantum Monte Carlo (DQMC) simulations [58]. The effective model including up to 4-body interactions takes the form

$$E_{\text{eff}}(S) \sim J_0 + \sum_{ij} g_{ij} \vec{s}_i \cdot \vec{s}_j + \sum_{ijkl} g_{ijkl} (\vec{s}_i \cdot \vec{s}_j) (\vec{s}_k \cdot \vec{s}_l). \quad (3)$$

Here, the dot products include all pairs of spins on the lattice, including self-interactions. The perturbative approach faces a fundamental dilemma: truncating at low orders fails to capture the full physics, while including higher-order terms leads to numerical divergence due to the factorial growth in the number of terms. EFNN addresses this challenge through renormalization.

The spin interactions in Eq. (3) are exclusively expressed as dot products to satisfy the $O(3)$ symmetry of Eq. (2). Inspired by this symmetry, we incorporate symmetrization layers into the EFNN architecture, depicted in Fig. 3. The symmetrization is achieved by summing dot products of each channel of S_0 after convolution:

$$T_j(S_0) = \sum_{k=x,y,z} \text{conv}(S_{0,k}) \odot \text{conv}(S_{0,k}), \quad j = 0, 1, \dots, n.$$

Here, each $S_{0,k} \in \mathbb{R}^{N \times N}$ is convolved into $\mathbb{R}^{C \times N \times N}$. Supplementary Material [51] details the convolution process and proves that T_j remains invariant under $O(3)$ transformations. As shown in Fig. 4(a), in the first FP layer, F_1 and S_1 are initialized as

$$F_1 = f_0(T_0(S_0)), \quad S_1 = g_1(T_1(S_0)) \odot F_1.$$

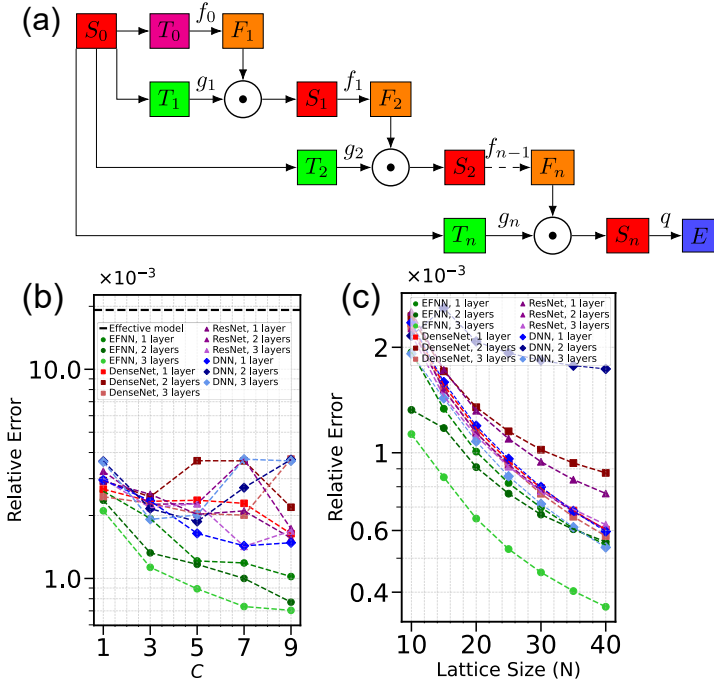


FIG. 4. Relative error of EFNNs. (a) Architecture of EFNN incorporating symmetrization layers T_j , $j = 0, 1, \dots, n$. (b) Performance of EFNNs, DenseNets, ResNets, DNNs and effective model on a test set with lattice size $N = 10$, for channel numbers $C = 1, 3, 5, 7, 9$. (c) Generalization performance of networks trained on 10×10 lattices ($C = 3$) when applied to larger systems.

For subsequent layers $j = 2, \dots, n$, the effective field and quasi-particle layers are

$$F_j = f_j(S_{j-1}), S_j = g_j(T_j(S_0)) \odot F_j.$$

The mappings f_j and g_k consist of a convolutional layer, a tanh activation, and another convolutional layer. For the mapping $q(S_n) = E$, the final quasi-particle layer S_n is convolved into a single-channel matrix, and an element-wise summation is performed to produce the scalar energy prediction E , see Supplementary Material [51]. The layer dimensions are as follows: input layer $S_0 \in \mathbb{R}^{3 \times N \times N}$, intermediate layers $F_j, S_j \in \mathbb{R}^{C \times N \times N}$, for $j = 1, \dots, n$, and output $E = q(S_n) \in \mathbb{R}$. For comparison, we also incorporate symmetrization layers and final summation q into DenseNet, ResNet, and DNN architectures, detailed in Supplementary Material [51].

We generate a total of 2×10^6 data points and split them into 80% for training and 20% for testing. These data are obtained by exact diagonalization of the Hamiltonian in Eq. (2) with chemical potential. For the effective model in Eq. (3), we perform linear regression to obtain the coefficients. While the full effective model would require 12758826 parameters, we reduce this to 213201 by restricting interactions within each 5×5 tile. The EFNNs, DenseNets, ResNets, and DNNs with symmetrization are trained using networks

with $C = 1, 3, 5, 7, 9$ channels and $n = 1, 2, 3$ layers, with parameter counts ranging from 200 to 30000. As shown in Fig. 4(b), the effective model achieves a relative error of approximately 2×10^{-2} , whereas the neural networks achieve relative errors on the order of 10^{-3} —approximately six times better using significantly fewer parameters. Among the neural networks, EFNNs with 1, 2, and 3 layers consistently outperform all other architectures, with some overlap observed between 1-layer EFNNs and 3-layer DNNs, as well as 1-, 2-, and 3-layer DenseNets at $C = 1, 3$. For EFNNs, the error systematically decreases as C increases and as the number of layers increases from 1 to 3. This superior performance with fewer parameters shows that the EFNNs possess inherent renormalization capabilities beyond simple parameter fitting.

We next test the generalization capability of these neural networks trained on 10×10 lattices by evaluating their performance on systems up to 40×40 . We select networks with $C = 3$ channels as a representative configuration and evaluate EFNN, DenseNet, ResNet, and DNN architectures across this range of lattice sizes. The convolution operations with padding under periodic boundary conditions (PBC) effectively capture interactions between localized and neighboring spins. As shown in Fig. 4(c), all neural network architectures show improved performance on larger lattices, with relative errors decreasing as the system size increases from 10×10 to 40×40 . The EFNNs exhibit the best extrapolation capability and renormalization ability: the 3-layer EFNN achieves the lowest errors across all lattice sizes, reaching a remarkable relative error of approximately 4×10^{-4} at $N = 40$. The 2-layer EFNN mostly outperforms the 1-layer EFNN, while among non-EFNN architectures, only the 3-layer DNN has comparable performance to the 1-layer EFNN. All other configurations consistently produce higher errors, confirming EFNN’s superior ability to capture scale-invariant features. Notably, as demonstrated in Supplementary Material [51], for $N = 40$, EFNN achieves 10^3 speed-up compared to ED.

We give some discussions and conclude this paper. In all three case studies—the classical 3-spin infinite-range model, continuous classical Heisenberg system, and quantum double exchange model—EFNNs consistently outperform DenseNets, ResNets, DNNs, and the effective model, achieving the lowest errors. Particularly striking is EFNN’s ability to generalize: trained on 10×10 lattices, it accurately predicted energies for systems as large as 40×40 , while DenseNets, ResNets, and standard DNNs struggle with this extrapolation task. This superior performance isn’t accidental—it stems from EFNN’s mathematical foundation in continued functions. While conventional architectures like DenseNet and ResNet were designed through trial and error with various architectural innovations, EFNN’s structure directly implements continued functions, a mathematical framework that naturally captures many-body interactions up to infinite order. More importantly, for a perturbative ex-

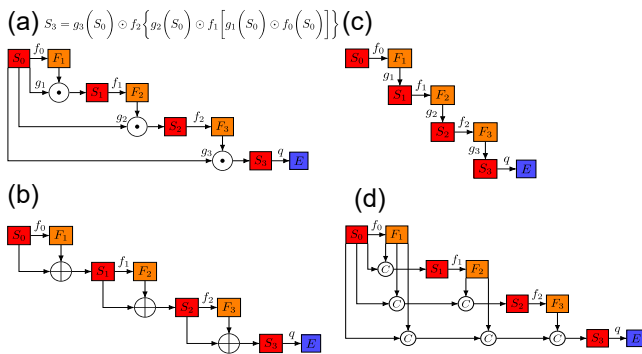


FIG. 5. Comparison of neural network structures. (a) In an EFNN, the initial layer S_0 is recursively integrated into every quasi-particle layer. After a mapping, S_0 is multiplied with subsequent layers, forming a continued-function representation (see the equation above the figure). (b) A typical architecture of ResNet, only one skip connection starts from S_0 and summation is used, this is not a correct continued-function structure. (c) Removing the S_0 connections transforms an EFNN into a standard DNN, with no continued-function structure. (d) A typical architecture of DenseNet, \textcircled{C} is concatenation operation, this is not a correct continued-function structure.

pansion like Eq. (3), EFNN selects the most relevant terms via training, and expresses these terms in nonlinear continued function structure. Fig. 5 compares these structures, demonstrating that only EFNN (Fig. 5(a)) possesses the correct continued function structure. The Supplementary Material [51] provides a detailed mathematical explanation of why EFNN implements continued functions while ResNet and DenseNet do not. A special case of continued functions is the Padé approximant, which takes the form of a continued fraction and is ubiquitously used throughout physics and numerical methods for its rapid convergence, strong extrapolation capability, and compact representation [59]. Continued functions generalize continued fractions by replacing the inversion operation with generic nonlinear functions. Here, we use \tanh activation functions instead of inverses, which makes EFNN trainable through standard backpropagation—something impossible with traditional Padé approximants due to gradient singularities. This simple substitution preserves the mathematical power of continued functions while enabling practical neural network training. Notably, EFNN actually implements self-similar approximation [60], a powerful mathematical framework that has been successfully applied

across diverse fields including high energy physics [61–65], condensed matter physics [66, 67], quantum mechanics [60, 64, 68–72], quantum field theory [60, 73–75], and applied mathematics [66, 76–85]. Previously, applying self-similar approximation required tedious manual calculations to obtain order by order matching; EFNN changes this by automating the process through neural network optimization. EFNN’s self-similar structure also naturally comes from renormalization group equation, as detailed in the Supplementary Material [51].

In conclusion, we have developed EFNN, a neural network architecture inspired by field theory that captures high-order interactions in both classical and quantum models. The key to EFNN’s success lies in how it recursively refines effective fields and constructs quasi-particles to encode complex many-body effects. This partitioning into field and quasi-particle layers provides clear physical interpretation while maintaining computational efficiency. As we showed, the connections from the true particle layer S_0 to the quasi-particle layers create a continued function structure with renormalization properties similar to Padé approximants. What EFNN actually implements is self-similar approximation—a powerful mathematical technique that has been widely used in physics but previously required manual calculations for each problem. Once properly trained, this architecture learns effective representations that accurately predict energies even for systems with complicated many-body interactions. Our tests on three diverse systems—the classical 3-spin infinite-range model, continuous classical Heisenberg spin system, and quantum double exchange model—demonstrate that EFNN consistently outperforms DenseNet, ResNet, and standard DNNs. Most remarkably, EFNNs trained on small systems improve accuracy on larger ones, opening possibilities for training on expensive DFT data from small lattices then inferring on much larger systems. Looking ahead, we plan to develop theoretical error bounds and apply EFNN to other challenging problems in physics.

DATA AVAILABILITY

The data that support the findings of this study are openly available in Zenodo at Ref. [86].

Acknowledgments—This work is supported by the Hong Kong Research Grants Council (16306220) and National Key R&D Program of China (2021YFA1401500). Y.Z. is supported by the Max Planck Partner lab on quantum materials from Max Planck Institute Chemical Physics of Solids.

-
- [1] J. Carrasquilla and R. G. Melko, Machine learning phases of matter, *Nature Physics* **13**, 431 (2017).
 [2] K. Ch’ng, J. Carrasquilla, R. G. Melko, and E. Khatami, Machine Learning Phases of Strongly Correlated

- Fermions, *Phys. Rev. X* **7**, 031038 (2017).
 [3] I. A. Iakovlev, O. M. Sotnikov, and V. V. Mazurenko, Supervised learning approach for recognizing magnetic skyrmion phases, *Phys. Rev. B* **98**, 174411 (2018).

- [4] L. Wang, Discovering phase transitions with unsupervised learning, *Phys. Rev. B* **94**, 195105 (2016).
- [5] E. P. L. van Nieuwenburg, Y.-H. Liu, and S. D. Huber, Learning phase transitions by confusion, *Nature Physics* **13**, 435 (2017).
- [6] K. Ch'ng, N. Vazquez, and E. Khatami, Unsupervised machine learning account of magnetic transitions in the Hubbard model, *Phys. Rev. E* **97**, 013306 (2018).
- [7] J. F. Rodriguez-Nieva and M. S. Scheurer, Identifying topological order through unsupervised machine learning, *Nature Physics* **15**, 790 (2019).
- [8] J. Arnold, F. Schäfer, M. Žonda, and A. U. J. Lode, Interpretable and unsupervised phase classification, *Phys. Rev. Res.* **3**, 033052 (2021).
- [9] G. Carleo and M. Troyer, Solving the quantum many-body problem with artificial neural networks, *Science* **355**, 602 (2017).
- [10] Y. Nomura, A. S. Darmawan, Y. Yamaji, and M. Imada, Restricted Boltzmann machine learning for solving strongly correlated quantum systems, *Phys. Rev. B* **96**, 205152 (2017).
- [11] K. Choo, G. Carleo, N. Regnault, and T. Neupert, Symmetries and Many-Body Excitations with Neural-Network Quantum States, *Phys. Rev. Lett.* **121**, 167204 (2018).
- [12] N. Yoshioka and R. Hamazaki, Constructing neural stationary states for open quantum many-body systems, *Phys. Rev. B* **99**, 214306 (2019).
- [13] J. Carrasquilla, G. Torlai, R. G. Melko, and L. Aolita, Reconstructing quantum states with generative models, *Nature Machine Intelligence* **1**, 155 (2019).
- [14] J. Liu, Y. Qi, Z. Y. Meng, and L. Fu, Self-learning Monte Carlo method, *Phys. Rev. B* **95**, 041101 (2017).
- [15] J. Liu, H. Shen, Y. Qi, Z. Y. Meng, and L. Fu, Self-learning Monte Carlo method and cumulative update in fermion systems, *Phys. Rev. B* **95**, 241104 (2017).
- [16] L. Huang and L. Wang, Accelerated Monte Carlo simulations with restricted Boltzmann machines, *Phys. Rev. B* **95**, 035105 (2017).
- [17] G. Kanwar, M. S. Albergó, D. Boyda, K. Cranmer, D. C. Hackett, S. Racanière, D. J. Rezende, and P. E. Shanahan, Equivariant Flow-Based Sampling for Lattice Gauge Theory, *Phys. Rev. Lett.* **125**, 121601 (2020).
- [18] J. Behler and M. Parrinello, Generalized Neural-Network Representation of High-Dimensional Potential-Energy Surfaces, *Phys. Rev. Lett.* **98**, 146401 (2007).
- [19] M. Rupp, A. Tkatchenko, K.-R. Müller, and O. A. von Lilienfeld, Fast and Accurate Modeling of Molecular Atomization Energies with Machine Learning, *Phys. Rev. Lett.* **108**, 058301 (2012).
- [20] A. P. Bartók, R. Kondor, and G. Csányi, On representing chemical environments, *Phys. Rev. B* **87**, 184115 (2013).
- [21] J. Behler, Constructing high-dimensional neural network potentials: A tutorial review, *International Journal of Quantum Chemistry* **115**, 1032 (2015).
- [22] D. Marchand, A. Jain, A. Glensk, and W. A. Curtin, Machine learning for metallurgy I. A neural-network potential for Al-Cu, *Phys. Rev. Mater.* **4**, 103601 (2020).
- [23] C. Fan, M. Shen, Z. Nussinov, Z. Liu, Y. Sun, and Y.-Y. Liu, Searching for spin glass ground states through deep reinforcement learning, *Nature Communications* **14**, 725 (2023).
- [24] K. Mills and I. Tamblin, Deep neural networks for direct, featureless learning through observation: The case of two-dimensional spin models, *Phys. Rev. E* **97**, 032119 (2018).
- [25] J.-L. Wu, H. Xiao, and E. Paterson, Physics-informed machine learning approach for augmenting turbulence models: A comprehensive framework, *Phys. Rev. Fluids* **3**, 074602 (2018).
- [26] M. Raissi, P. Perdikaris, and G. Karniadakis, Physics-informed neural networks: A deep learning framework for solving forward and inverse problems involving nonlinear partial differential equations, *Journal of Computational Physics* **378**, 686 (2019).
- [27] S. L. Brunton, B. R. Noack, and P. Koumoutsakos, Machine Learning for Fluid Mechanics, *Annual Review of Fluid Mechanics* **52**, 477 (2020).
- [28] L. Lu, X. Meng, Z. Mao, and G. E. Karniadakis, DeepXDE: A Deep Learning Library for Solving Differential Equations, *SIAM Review* **63**, 208 (2021).
- [29] M. Mattheakis, P. Protopapas, D. Sondak, M. D. Giovanni, and E. Kaxiras, Physical Symmetries Embedded in Neural Networks (2020).
- [30] A. Bogatskiy, B. Anderson, J. Offermann, M. Roussi, D. Miller, and R. Kondor, Lorentz group equivariant neural network for particle physics, in *Proceedings of the 37th International Conference on Machine Learning*, Proceedings of Machine Learning Research, Vol. 119 (PMLR, 2020) pp. 992–1002.
- [31] L. Yang, D. Zhang, and G. E. Karniadakis, Physics-Informed Generative Adversarial Networks for Stochastic Differential Equations, *SIAM Journal on Scientific Computing* **42**, A292 (2020).
- [32] K. Mills, K. Ryczko, I. Luchak, A. Domurad, C. Beeler, and I. Tamblin, Extensive deep neural networks for transferring small scale learning to large scale systems, *Chem. Sci.* **10**, 4129 (2019).
- [33] S. Batzner, A. Musaelian, L. Sun, M. Geiger, J. P. Mailoa, M. Kornbluth, N. Molinari, T. E. Smidt, and B. Kozinsky, E(3)-equivariant graph neural networks for data-efficient and accurate interatomic potentials, *Nature Communications* **13**, 2453 (2022).
- [34] F. Xie, T. Lu, S. Meng, and M. Liu, GPTFF: A high-accuracy out-of-the-box universal AI force field for arbitrary inorganic materials, *Science Bulletin* **69**, 3525 (2024).
- [35] Y. Han, J. Wang, C. Ding, H. Gao, S. Pan, Q. Jia, and J. Sun, Prediction of surface reconstructions using MAGUS, *The Journal of Chemical Physics* **158**, 174109 (2023).
- [36] Y. Zhong, H. Yu, X. Gong, and H. Xiang, A General Tensor Prediction Framework Based on Graph Neural Networks, *The Journal of Physical Chemistry Letters* **14**, 6339 (2023).
- [37] H. Gao, J. Wang, Y. Han, and J. Sun, Enhancing crystal structure prediction by decomposition and evolution schemes based on graph theory, *Fundamental Research* **1**, 466 (2021).
- [38] J. Wang, H. Gao, Y. Han, C. Ding, S. Pan, Y. Wang, Q. Jia, H.-T. Wang, D. Xing, and J. Sun, MAGUS: machine learning and graph theory assisted universal structure searcher, *National Science Review* **10**, nwad128 (2023).
- [39] H. Yu, Y. Zhong, L. Hong, C. Xu, W. Ren, X. Gong, and H. Xiang, Spin-dependent graph neural network potential for magnetic materials, *Phys. Rev. B* **109**, 144426 (2024).
- [40] S.-H. Li and L. Wang, Neural Network Renormalization

- Group, Phys. Rev. Lett. **121**, 260601 (2018).
- [41] Y. Zhong, S. Liu, B. Zhang, Z. Tao, Y. Sun, W. Chu, X.-G. Gong, J.-H. Yang, and H. Xiang, Accelerating the calculation of electron–phonon coupling strength with machine learning, Nature Computational Science **4**, 615 (2024).
- [42] C. Zhang, Y. Zhong, Z.-G. Tao, X. Qing, H. Shang, Z. Lan, O. V. Prezhdo, X.-G. Gong, W. Chu, and H. Xiang, Advancing nonadiabatic molecular dynamics simulations for solids: Achieving supreme accuracy and efficiency with machine learning (2024).
- [43] H. Yu, C. Xu, X. Li, F. Lou, L. Bellaiche, Z. Hu, X. Gong, and H. Xiang, Complex spin Hamiltonian represented by an artificial neural network, Phys. Rev. B **105**, 174422 (2022).
- [44] T. Lv, Z. Zhong, Y. Liang, F. Li, J. Huang, and R. Zheng, Deep Charge: Deep learning model of electron density from a one-shot density functional theory calculation, Phys. Rev. B **108**, 235159 (2023).
- [45] Z. Fan, Y. Wang, P. Ying, K. Song, J. Wang, Y. Wang, Z. Zeng, K. Xu, E. Lindgren, J. M. Rahm, A. J. Gabourie, J. Liu, H. Dong, J. Wu, Y. Chen, Z. Zhong, J. Sun, P. Erhart, Y. Su, and T. Ala-Nissila, GPUMD: A package for constructing accurate machine-learned potentials and performing highly efficient atomistic simulations, The Journal of Chemical Physics **157**, 114801 (2022).
- [46] X.-T. Xie, Z.-X. Yang, D. Chen, Y.-F. Shi, P.-L. Kang, S. Ma, Y.-F. Li, C. Shang, and Z.-P. Liu, LASP to the Future of Atomic Simulation: Intelligence and Automation, Precision Chemistry **2**, 612 (2024).
- [47] Z.-X. Yang, X.-T. Xie, P.-L. Kang, Z.-X. Wang, C. Shang, and Z.-P. Liu, Many-Body Function Corrected Neural Network with Atomic Attention (MBNN-att) for Molecular Property Prediction, Journal of Chemical Theory and Computation **20**, 6717 (2024).
- [48] L. Barroso-Luque, M. Shuaibi, X. Fu, B. M. Wood, M. Dzamba, M. Gao, A. Rizvi, C. L. Zitnick, and Z. W. Ulissi, Open Materials 2024 (OMat24) Inorganic Materials Dataset and Models (2024).
- [49] Y. Han, J. Wang, C. Ding, H. Gao, S. Pan, Q. Jia, and J. Sun, Prediction of surface reconstructions using MAGUS, The Journal of Chemical Physics **158**, 174109 (2023).
- [50] D. Pfau, J. S. Spencer, A. G. D. G. Matthews, and W. M. C. Foulkes, Ab initio solution of the many-electron Schrödinger equation with deep neural networks, Phys. Rev. Res. **2**, 033429 (2020).
- [51] Supplemental Material of Effective Field Neural Networks.
- [52] C. Zener, Interaction between the d -Shells in the Transition Metals. II. Ferromagnetic Compounds of Manganese with Perovskite Structure, Phys. Rev. **82**, 403 (1951).
- [53] P. W. Anderson and H. Hasegawa, Considerations on Double Exchange, Phys. Rev. **100**, 675 (1955).
- [54] P. G. de Gennes, Effects of Double Exchange in Magnetic Crystals, Phys. Rev. **118**, 141 (1960).
- [55] M. A. Ruderman and C. Kittel, Indirect Exchange Coupling of Nuclear Magnetic Moments by Conduction Electrons, Phys. Rev. **96**, 99 (1954).
- [56] T. Kasuya, A Theory of Metallic Ferro- and Antiferromagnetism on Zener’s Model, Progress of Theoretical Physics **16**, 45 (1956).
- [57] K. Yosida, Magnetic Properties of Cu-Mn Alloys, Phys. Rev. **106**, 893 (1957).
- [58] J. Liu, H. Shen, Y. Qi, Z. Y. Meng, and L. Fu, Self-learning Monte Carlo method and cumulative update in fermion systems, Phys. Rev. B **95**, 241104 (2017).
- [59] G. A. Baker and P. Graves-Morris, *Padé Approximants*, 2nd ed. (Cambridge University Press, Cambridge, 1996).
- [60] V. I. Yukalov, Interplay between Approximation Theory and Renormalization Group, Physics of Particles and Nuclei **50**, 141 (2019).
- [61] V. Abhignan and R. Sankaranarayanan, Continued Functions and Perturbation Series: Simple Tools for Convergence of Diverging Series in $O(n)$ -Symmetric ϕ^4 Field Theory at Weak Coupling Limit, Journal of Statistical Physics **183**, 4 (2021).
- [62] V. Yukalov and E. Yukalova, Higher orders of self-similar approximations for thermodynamic potentials, Physica A: Statistical Mechanics and its Applications **206**, 553 (1994).
- [63] V. Yukalov and E. Yukalova, Self-similar approximations for thermodynamic potentials, Physica A: Statistical Mechanics and its Applications **198**, 573 (1993).
- [64] V. Yukalov and E. Yukalova, Self-Similar Perturbation Theory, Annals of Physics **277**, 219 (1999).
- [65] C. Quigg and J. L. Rosner, Quantum mechanics with applications to quarkonium, Physics Reports **56**, 167 (1979).
- [66] V. I. Yukalov and S. Gluzman, Self-similar bootstrap of divergent series, Physical Review E **55**, 6552 (1997).
- [67] S. Gluzman and V. I. Yukalov, Critical indices from self-similar root approximants, The European Physical Journal Plus **132**, 535 (2017).
- [68] V. Yukalov and E. Yukalova, Critical temperature in weakly interacting multicomponent field theory, in *EPJ Web of Conferences*, Vol. 138 (EDP Sciences, 2017) p. 03011.
- [69] V. I. Yukalov and E. P. Yukalova, Bose–Einstein condensation temperature of weakly interacting atoms, Laser Physics Letters **14**, 073001 (2017).
- [70] V. Yukalov and E. Yukalova, Temporal dynamics in perturbation theory, Physica A: Statistical Mechanics and its Applications **225**, 336 (1996).
- [71] E. P. Yukalova and V. I. Yukalov, *Calculation of eigenvalues of Schrödinger operators for arbitrary coupling*, Tech. Rep. (Joint Institute for Nuclear Research (JINR), Dubna, Russia, 1992).
- [72] S. Gluzman and V. I. Yukalov, Effective Summation and Interpolation of Series by Self-Similar Root Approximants, Mathematics **3**, 510 (2015).
- [73] V. I. Yukalov and E. Yukalova, Phase transition in multicomponent field theory at finite temperature, in *PoS*, Vol. Baldin ISHEPP XXII (Sissa Medialab, 2015) p. 080.
- [74] V. I. Yukalov and E. P. Yukalova, Calculation of critical exponents by self-similar factor approximants, The European Physical Journal B **55**, 93 (2007).
- [75] V. I. Yukalov and E. P. Yukalova, Equation of State in Quantum Chromodynamics (2000).
- [76] E. Yukalova, V. Yukalov, and S. Gluzman, Self-similar factor approximants for evolution equations and boundary-value problems, Annals of Physics **323**, 3074 (2008).
- [77] V. Yukalov, Self-similar extrapolation of asymptotic series and forecasting for time series, Modern Physics Letters B **14**, 791 (2000).
- [78] S. Gluzman and V. Yukalov, Resummation Methods for

- Analyzing Time Series, *Modern Physics Letters B* **12**, 61 (1998).
- [79] S. Gluzman and V. Yukalov, Renormalization Group Analysis of October Market Crashes, *Modern Physics Letters B* **12**, 75 (1998).
- [80] S. Gluzman and V. Yukalov, Booms and Crashes in Self-Similar Markets (1998).
- [81] V. Yukalov and S. Gluzman, Weighted Fixed Points in Self-Similar Analysis of Time Series, *International Journal of Modern Physics B* **13**, 1463 (1999).
- [82] V. Yukalov, Self-Similar Approach to Market Analysis, *The European Physical Journal B - Condensed Matter and Complex Systems* **20**, 609 (2001).
- [83] S. Gluzman, D. Sornette, and V. Yukalov, Reconstructing Generalized Exponential Laws By Self-Similar Exponential Approximants, *International Journal of Modern Physics C* **14**, 509 (2003).
- [84] V. I. Yukalov and E. P. Yukalova, Cooperative Electromagnetic Effects (2000).
- [85] V. Yukalov, Principle of Pattern Selection for Nonequilibrium Phenomena, *Physics Letters A* **284**, 91 (2001).
- [86] X. Liu, Y. Zhao, C. Y. Wan, Y. Zhang, and J. Liu, Data for: Renormalization-inspired effective field neural networks for scalable modeling of classical and quantum many-body systems (2025).

Supplemental Information of Effective Field Neural Networks

In this supplementary information, we present the complete workflow of EFNN with symmetrization for the quantum double exchange model in Section I. We introduce the basics of Padé approximation, continued fractions, and continued functions in Section II, and demonstrate that EFNN implements a continued function, while ResNet, DenseNet and DNN are not continued functions. In Section III, we derive the structure of EFNN from the renormalization group (RG) equation. In Section IV, we show that the convolution layer ensures the system's invariance under the point group $O(3)$. In Section V, we present the adapted architectures of ResNet, DenseNet, and DNN for energy fitting of the quantum double exchange model. In Section VI, we break down the details of DQMC, and demonstrate how EFNN solves the computational bottleneck problem in DQMC for quantum double exchange model. We report the speed-up of EFNN against ED. In Section VII, we report the distributions of EFNN's predictions, and the ground truth data, for quantum double exchange model, demonstrating that the accuracy of EFNN.

I. COMPUTATIONAL WORKFLOW OF EFNNs WITH SYMMETRIZATION

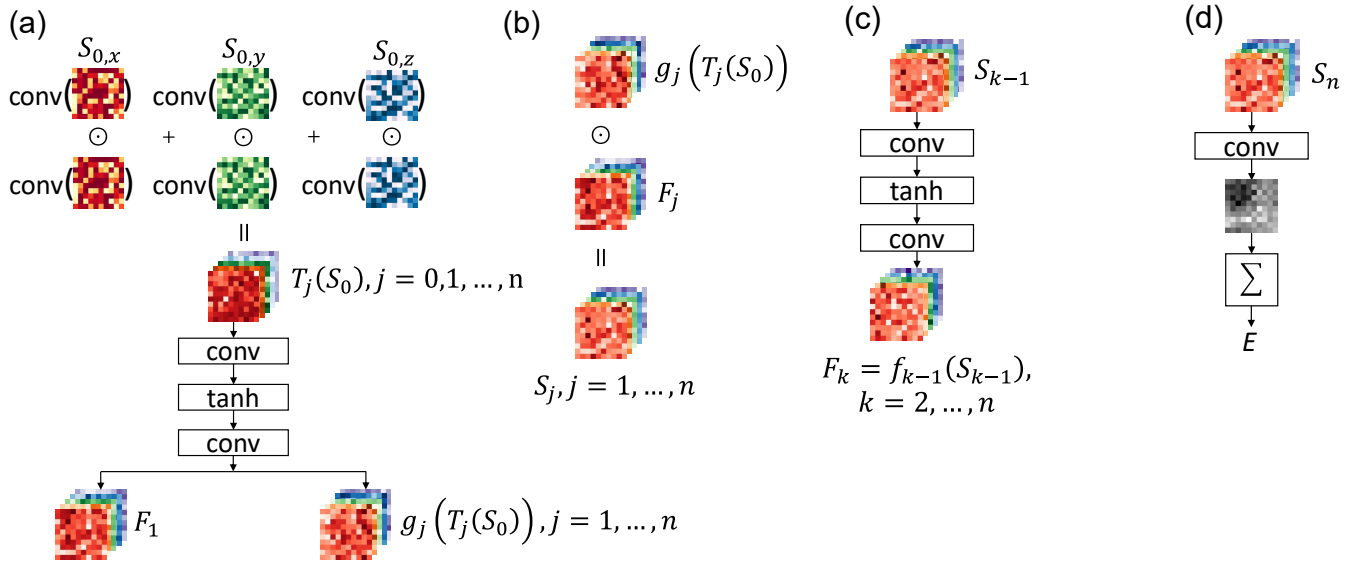


FIG. 1. Computational workflow of EFNNs with symmetrization

In this section, we present the complete workflow of EFNN with symmetrization for the quantum double exchange model. Fig.1(a) illustrates the symmetrization process: each of the three channels of S_0 ($S_{0,x}$, $S_{0,y}$, $S_{0,z}$) undergoes convolution and element-wise multiplication within the same channel. The resulting products are summed to form the symmetrization layer $T_j(S_0)$. Subsequently, $T_j(S_0)$ is passed through a sequence of layers—convolution, tanh activation, and convolution—to produce F_1 for $j = 0$ or $g_j(T_j(S_0))$ for $j = 1, \dots, n$. Fig. 1(a) is Fig. 3 in the main text. Fig. 1(b) shows the generation of quasi-particle layers: the transformed symmetrization layer $g_j(T_j(S_0))$ is element-wise multiplied with the effective field layer F_j , yielding the quasi-particle layer S_j for $j = 1, \dots, n$. Fig. 1(c) depicts the transformation to effective field layers: each quasi-particle layer S_{k-1} is processed through convolution, tanh activation, and convolution to generate the effective field layer F_k for $k = 2, \dots, n$. Fig. 1(d) illustrates the energy evaluation: the final quasi-particle layer S_n is transformed into a single-channel matrix, and an element-wise summation of this matrix yields the scalar energy prediction E . These visualizations are generated after training the model with $C = 5$ channels and $n = 2$ layers, using the 576th sample from the test set as input S_0 .

II. MATHEMATICAL DETAILS OF DENSENET, RESNET, DNN

In this section, we describe the mathematical structures of EFNN, ResNet, DenseNet, and DNN.

We denote the input spins as $S_0 \in \mathbb{R}^N$.

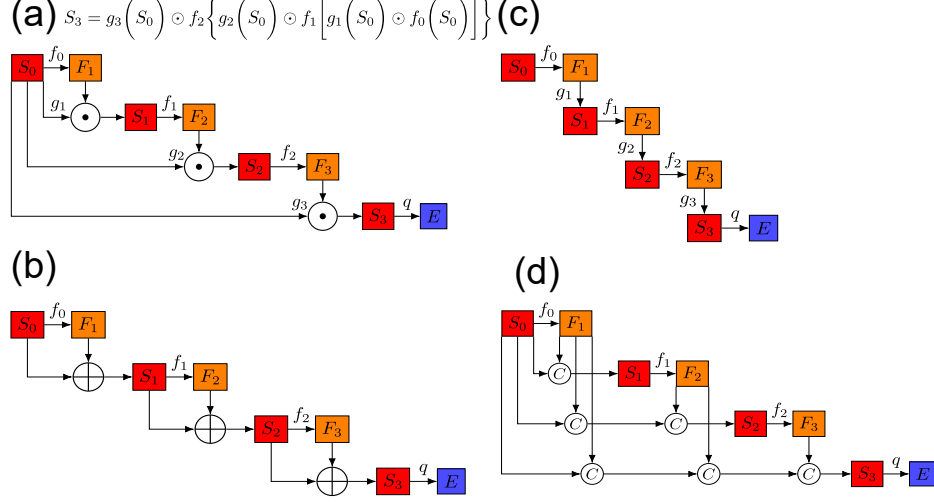


FIG. 2. Comparison of structures of (a) EFNN, (b) ResNet, (c) DNN, and (d) DenseNet

Why EFNN is a continued function

In Fig. 2(a), the functions g_k , $k = 1, 2, 3$, f_j , $j = 0, 1, 2$, all have the forms of a composition of a linear mapping \odot $\tanh \odot$ linear mapping. We denote

$$g_k(z) = \beta_k \tanh(\gamma_k z + \delta_k) + \varphi_k, \quad k = 1, 2, 3, \quad (1)$$

$$f_j(z) = d_j + c_j \tanh(A_j z + b_j), \quad j = 0, 1, 2. \quad (2)$$

The quasi-particle layers in EFNN form a nested structure that implements a continued function. For instance, the third quasi-particle layer is expressed as:

$$S_3 = g_3 \left(S_0 \right) \odot f_2 \left\{ g_2 \left(S_0 \right) \odot f_1 \left[g_1 \left(S_0 \right) \odot f_0 \left(S_0 \right) \right] \right\}, \quad (3)$$

where \odot denotes the Hadamard (element-wise) product.

To illustrate why this structure constitutes a continued function, we draw an analogy with Padé approximants, which can be expressed as continued fractions—a special case of continued functions.

In physics and applied mathematics, perturbative series naturally express physical interactions to arbitrary order. However, these series have a fundamental dilemma: truncating at low order fails to capture the complete physics, while including higher-order terms typically leads to divergence. Renormalization provides the solution to this problem, with Padé approximants being the most widely used numerical scheme for transforming divergent series into convergent expressions. To match a perturbative series $f(x) \sim c_0 + c_1 x + c_2 x^2 + \dots$ with a Padé approximant $\frac{P_M(x)}{Q_M(x)}$, one equates truncated $c_0 + c_1 x + c_2 x^2 + \dots$ with the rational function $\frac{P_M(x)}{Q_M(x)}$, then deals with the algebraic equation $(c_0 + c_1 x + c_2 x^2 + \dots)Q_M(x) = P_M(x)$. M is the order of the polynomial. The approximation accuracy typically improves as $M \rightarrow \infty$. Examples of continued fraction:

- Exponential function:

$$e^x \sim 1 + \frac{1}{1!}x + \frac{1}{2!}x^2 + \frac{1}{3!}x^3 + \frac{1}{4!}x^4 + \dots = 1 + \frac{x}{1 - \frac{x}{2 + x - \frac{2x}{3 + x - \frac{3x}{4 + x - \dots}}}}. \quad (4)$$

- Natural logarithm:

$$\log(1+x) \sim x - \frac{1}{2}x^2 + \frac{1}{3}x^3 - \frac{1}{4}x^4 + \dots = \frac{x}{1 + \frac{1^2x}{2 + \frac{1^2x}{3 + \frac{2^2x}{4 + \dots}}}}. \quad (5)$$

The Padé approximant for e^x in Eq. (4) has everyday application throughout numerical analysis, since this is how matrix exponential is computed in various programming languages [1], for example, the `expm` in Python, Mathematica, and MATLAB. In Eq. (5), the perturbative series diverges for $x \geq 1$, however, the Padé approximant always converges and captures well the value of $\log(1+x)$. The continued fraction can be naturally generalized, by replacing the inverse operation with other nonlinear functions. Examples of continued function [2]:

- $C_N(z) = c_0 \exp(c_1 z \exp(c_2 z \dots \exp(c_N z)))$,
- $C_N(z) = c_0 \sqrt{1 + c_1 z \sqrt{1 + c_2 z \sqrt{1 + \dots c_{N-1} z \sqrt{1 + c_N z}}}}$,
- $C_N(z) = \log(c_0 + z \log(c_1 + z \log(c_2 + \dots z \log(c_N + z))))$.

To see why EFNN is a continued function, we first turn to a simpler case by requiring $S_0 \in \mathbb{R}$. We let $f_j(z) = d_j + \frac{c_j}{b_j + A_j z}$, then S_3 in Eq. (3) becomes:

$$S_3 = g_3(S_0)d_2 + \frac{g_3(S_0)c_2}{b_2 + A_2 g_2(S_0)d_1 + \frac{A_2 g_2(S_0)c_1}{b_1 + A_1 g_1(S_0)d_0 + \frac{A_1 g_1(S_0)c_0}{b_0 + A_0 S_0}}}. \quad (6)$$

Since S_0 is actually a vector, and rational functions always introduce fictitious poles, we would like to replace the inverse function with \tanh , using Eq. (2). Then the neural network implementation with \tanh then gives us:

$$S_3 = g_3(S_0) \odot \left[d_2 + c_2 \tanh \left(b_2 + A_2 g_2(S_0) \odot \left[d_1 + c_1 \tanh \left(b_1 + A_1 g_1(S_0) \odot \left[d_0 + c_0 \tanh \left(b_0 + A_0 S_0 \right) \right] \right) \right] \right) \right]. \quad (7)$$

And we have fully demonstrated that S_3 is a continued function.

Note that in Eq. (7), S_3 is vector-valued, each component of S_3 , which is a finite value, contains infinite number of perturbation terms, as shown in Eq. (8).

$$\sum_{n_1, n_2, \dots, n_N=0}^{\infty} a_{n_1 n_2 \dots n_N} [S_0^{(1)}]^{n_1} [S_0^{(2)}]^{n_2} \dots [S_0^{(N)}]^{n_N}. \quad (8)$$

Why ResNet, DenseNet, and DNN are not continued function

For DNN, as shown in Fig. 2(c), the mapping $S_0 \mapsto F_1 \mapsto S_1 \mapsto F_2 \mapsto \dots \mapsto S_3 = g_3(f_2(g_2(f_1(g_1 f_0(S_0))))))$, does not contain any skip connections, as required by continued function. Therefore it is apparent that DNN is not a continued function.

For ResNet,

$$F_j = f_j(S_{j-1}), \quad (9)$$

$$S_j = S_{j-1} \oplus F_j, j = 1, 2, 3, \quad (10)$$

\oplus is element-wise addition in Fig. 2(b). Then

$$S_3 = S_0 + f_0(S_0) + f_1[S_0 + f_0(S_0)] + f_2 \left\{ S_0 + f_0(S_0) + f_1[S_0 + f_0(S_0)] \right\}. \quad (11)$$

f_j is nonlinear. Clearly Eq. (11) is not a correct continued function. The correct form would be:

$$S_3 = S_0 + f_2[S_0 + f_1(S_0 + f_0(S_0))]. \quad (12)$$

There are too many redundant terms in Eq. (11). The expression in Eq. (12) has the structure of Fig. 2(a), with \odot replaced by \oplus , and g_j set to identity.

For DenseNet, as shown in Fig. 2(d), \textcircled{C} is vector concatenation: for $x \in \mathbb{R}^a$, $y \in \mathbb{R}^b$, $x \textcircled{C} y = [x^\top, y^\top]^\top$. We take nonlinear functions f_j , the subsequent layer are:

$$F_1 = f_1(W_0 S_0 + b_1), \quad (13)$$

$$S_1 = \begin{bmatrix} S_0 \\ F_1 \end{bmatrix}, \quad (14)$$

$$F_2 = f_2 \left([W_{10}, W_{11}] \begin{bmatrix} S_0 \\ F_1 \end{bmatrix} + b_1 \right), \quad (15)$$

$$S_2 = \begin{bmatrix} S_0 \\ F_1 \\ F_2 \end{bmatrix}, \quad (16)$$

$$F_3 = f_3 \left([W_{20}, W_{21}, W_{22}] \begin{bmatrix} S_0 \\ F_1 \\ F_2 \end{bmatrix} + b_2 \right), \quad (17)$$

$$S_3 = \begin{bmatrix} S_0 \\ F_1 \\ F_2 \\ F_3 \end{bmatrix}. \quad (18)$$

The explicit expressions for F_1, F_2, F_3 read

$$F_1 = f_0(W_0 S_0 + b_0), \quad (19)$$

$$F_2 = f_1 \left[W_{10} S_0 + W_{11} f_0(W_0 S_0 + b_0) + b_1 \right], \quad (20)$$

$$F_3 = f_2 \left\{ W_{20} S_0 + W_{21} f_0(W_0 S_0 + b_0) + W_{22} f_1 \left[W_{10} S_0 + W_{11} f_0(W_0 S_0 + b_0) + b_1 \right] + b_2 \right\}. \quad (21)$$

The expression in Eq. (18) is not a correct continued function. The S_3 layer concatenates previous layers, a summation of S_3 's components gives energy, such complicated function cannot be interpreted, and S_0 is not properly renormalized.

III. FROM RENORMALIZATION GROUP EQUATION TO EFNN

In the previous section, we have explained that EFNN is a continued function. In this section, we show that the EFNN structure can be derived from a renormalization group (RG) equation, as all continued functions can be.

We follow the arguments in Refs. [3–5], to derive the EFNN structure from RG equation. The derivation proceeds in 4 major steps: Step 1, we transform the perturbative series using an algebraic prefactor, and obtain exponential renormalization through RG equation. Step 2, we apply nested renormalization to create the exponential self-similar approximant with hierarchical structure. Step 3, we replace unbounded functions with bounded tanh functions while preserving asymptotic properties. Step 4, we generalize from scalar to vector inputs using Hadamard products, yielding the final EFNN architecture.

Step 1: using algebraic transform to renormalize perturbative series through RG equation

We first use scalar $S_0 \in \mathbb{R}$, target function is $E(S_0)$, we know its perturbative series up to k -th order:

$$p_0(S_0) = a_0, \quad (22)$$

$$p_1(S_0) = a_0 + a_1 S_0, \quad (23)$$

$$\vdots \quad (24)$$

$$p_{k-1}(S_0) = a_0 + a_1 S_0 + \cdots + a_{k-1} S_0^{k-1}, \quad (25)$$

$$p_k(S_0) = a_0 + a_1 S_0 + \cdots + a_{k-1} S_0^{k-1} + a_k S_0^k. \quad (26)$$

We apply an algebraic transform to the above polynomials:

$$u_0 = S_0^\theta p_0(S_0) = a_0 S_0^\theta, \quad (27)$$

$$u_1 = S_0^\theta p_1(S_0) = a_0 S_0^\theta + a_1 S_0^{1+\theta}, \quad (28)$$

$$\vdots \quad (29)$$

$$u_{k-1}(S_0) = S_0^\theta p_{k-1}(S_0) = a_0 S_0^\theta + a_1 S_0^{1+\theta} + \cdots + a_{k-1} S_0^{\theta+k-1} \quad (30)$$

$$u_k(S_0) = S_0^\theta p_k(S_0) = a_0 S_0^\theta + a_1 S_0^{1+\theta} + \cdots + a_{k-1} S_0^{\theta+k-1} + a_k S_0^{\theta+k}. \quad (31)$$

We embed the discrete functions $\{u_j(S_0) : j \in \mathbb{N}\}$ into $\{u(t, S_0) : t \geq 0\}$, with $u_j(S_0) = u(j, S_0)$, since continuous variable is easier to deal with. t is interpreted as time. We let $u(0, S_0) = f$, and further denote $u(t, S_0)$ as $u(t, S_0, f)$, to show that the initial value of the flow is f , while the variable in physical space is S_0 . We assume that u satisfies the self-similar equation:

$$u(t_2 + t_1, S_0, f) = u(t_2, S_0, u(t_1, S_0, f)), \quad (32)$$

because we hope to find the fixed point solution u^* :

$$u(t, S_0, u^*(S_0)) = u^*(S_0), \quad (33)$$

to guarantee the best convergence when using variable S_0 [6], i.e., in the physical space. $u^*(S_0)$ does not depend on t , because it is already a fixed point solution. $u^*(S_0)$ does not depend on initial value f , because we hope that u^* is an attractor. Eq. (32) leads to the Lie equation:

$$\partial_t u(t, S_0, f) = v(u(t, S_0, f)), \quad (34)$$

the velocity is given by

$$v(u(t, S_0, f)) = \left. \partial_\epsilon u(\epsilon, S_0, u(t, S_0, f)) \right|_{\epsilon=0}. \quad (35)$$

Lie equation is exactly RG equation, when t is scaled as $t = \log \tau$:

$$\frac{\partial u}{\partial \log \tau} = v(u). \quad (36)$$

We can't obtain the fixed point solution u^* exactly, and need to compute the so called k -th order quasi-fixed point solution. We use the Euler scheme to approximate the velocity at $t = k$:

$$v(u(k, S_0, f)) \simeq u(k, S_0, f) - u(k-1, S_0, f) = a_k S_0^{\theta+k}. \quad (37)$$

We assume that starting from u_{k-1} , it takes time T_k to reach the k -th order quasi-fixed point u_k^* , integrating the Lie equation Eq. (34), we obtain:

$$\int_{u_{k-1}}^{u_k^*} \frac{du}{a_k \xi^{\theta+k}} = T_k. \quad (38)$$

The dummy variable ξ is in physical space, starting with S_0 for lower limit $u_{k-1}(S_0, f)$. We choose the renormalization map from physical space to function space as algebraic:

$$u = b\xi^\theta, \quad (39)$$

then

$$u_k^* = (u_{k-1}^{-\frac{k}{\theta}} - \frac{k}{\theta} \frac{a_k}{b^{1+\frac{k}{\theta}}} T_k)^{-\frac{\theta}{k}}. \quad (40)$$

We multiply the above equation by $S_0^{-\theta}$ to scale back, and obtain a renormalized value for $E(S_0)$:

$$\begin{aligned} E_k^*(S_0) &= S_0^{-\theta} u_k^* \\ &= p_{k-1}(S_0) \left[1 - \frac{k}{\theta} \frac{a_k}{b^{1+\frac{k}{\theta}}} T_k S_0^k p_{k-1}^{\frac{k}{\theta}}(S_0) \right]^{-\frac{\theta}{k}}. \end{aligned} \quad (41)$$

Starting from Eq. (41), by tuning values of θ, b, T_k , we can arrive at several continued function approximants, including Padé. Here, we let $\theta \rightarrow \infty$, and obtain

$$E_k^*(S_0) = p_{k-1}(S_0) \exp\left(\frac{a_k}{b} T_k S_0^k\right). \quad (42)$$

This is to say, this one-step renormalization is a map:

$$p_k(S_0) = a_0 + a_1 S_0 + \cdots + a_k S_0^k \mapsto E_k^*(S_0) = (a_0 + a_1 S_0 + \cdots + a_{k-1} S_0^{k-1}) \exp\left(\frac{a_k}{b} T_k S_0^k\right). \quad (43)$$

We repeat the renormalization process for the polynomial prefactor until only the affine term is left:

$$p_k(S_0) \mapsto (a_0 + a_1 S_0) \exp\left(\frac{a_2}{b} T_2 S_0^2 + \frac{a_3}{b} T_3 S_0^3 + \cdots + \frac{a_k}{b} T_k S_0^k\right). \quad (44)$$

Step 2: using nested renormalization to obtain exponential self-similar approximant

We use the exponential renormalization to renormalize the polynomial in the exponential part in Eq. (44), and always leave a linear term as a prefactor, we obtain the exponential self-similar approximant:

$$p_k(S_0) \mapsto (a_0 + a_1 S_0) \exp(b_1 S_0 \exp(b_2 S_0 \cdots \exp(b_{n_k} S_0))). \quad (45)$$

n_k is an integer depending on k . One often performs a perturbation analysis for the exponential self-similar approximant with the perturbative series to obtain the unknown coefficients b_1, b_2, \dots, b_{n_k} . Note that one may also include the linear term $a_1 S_0$ in the exponential, we have the freedom of not taking this approach, and we have numerically tested that this approach does not work well.

Step 3: further renormalization for exponential self-similar approximant

Since linear functions and exponential functions are not bounded, to achieve better convergence, we need to further renormalize the nested exponential in Eq. (45). Since we do not use order by order matching to determine the unknown coefficients, we can set n_k with a given integer. We take $n_k = 3$ as an example. To further renormalize, we proceed in 5 substeps. We denote the exponential continued function as

$$\Phi_1(S_0) = (\alpha_3 S_0 + \kappa_3) \exp(\alpha_2 S_0 \exp(\alpha_1 S_0 \exp(A_0 S_0))). \quad (46)$$

First, we scale and shift the exp function in $\Phi_1(S_0)$:

$$\begin{aligned} \Phi_1(S_0) &\mapsto \Phi_2(S_0) \\ &= (\alpha_3 S_0 + \kappa_3) \left[d'_2 + c_2 \exp \left(b_2 + \alpha_2 S_0 \left[d'_1 + c_1 \exp \left(b_1 + \alpha_1 S_0 \left[d'_0 + c_0 \exp \left(A_0 S_0 \right) \right] \right) \right] \right) \right]. \end{aligned} \quad (47)$$

Second, we shift the origin of S_0 in $\Phi_2(S_0)$:

$$\begin{aligned} \Phi_2(S_0) &\mapsto \Phi_3(S_0) \\ &= (\alpha_3 S_0 + \theta_3) \left[d'_2 + c_2 \exp \left(b_2 + (\alpha_2 S_0 + \theta_2) \left[d'_1 + c_1 \exp \left(b_1 + (\alpha_1 S_0 + \theta_1) \left[d'_0 + c_0 \exp \left(b_0 + A_0 S_0 \right) \right] \right) \right] \right) \right]. \end{aligned} \quad (48)$$

Third, renormalize exp by tanh. We know that $1 + \tanh(y) \sim \exp(y)$, when $|y|$ is small, and $\tanh(y)$ is bounded on \mathbb{R} . Therefore we replace $\exp(y)$ by $1 + \tanh(y)$:

$$\begin{aligned} \Phi_3(S_0) &\mapsto \Phi_4(S_0) \\ &= (\alpha_3 S_0 + \theta_3) \left[d_2 + c_2 \tanh \left(b_2 + (\alpha_2 S_0 + \theta_2) \left[d_1 + c_1 \tanh \left(b_1 + (\alpha_1 S_0 + \theta_1) \left[d_0 + c_0 \tanh \left(b_0 + A_0 S_0 \right) \right] \right) \right] \right) \right]. \end{aligned} \quad (49)$$

Fourth, renormalize the linear prefactors before tanh. Since $y \sim \tanh(y)$, when $|y|$ is small, we perform the following renormalizations:

$$\alpha_j S_0 + \theta_j \mapsto g_j(S_0) = \beta_j \tanh(\gamma_j S_0 + \delta_j) + \varphi_j, \quad j = 1, 2, 3. \quad (50)$$

Then

$$\begin{aligned} \Phi_4(S_0) &\mapsto \Phi_5(S_0) \\ &= g_3(S_0) \left[d_2 + c_2 \tanh \left(b_2 + g_2(S_0) \left[d_1 + c_1 \tanh \left(b_1 + g_1(S_0) \left[d_0 + c_0 \tanh \left(b_0 + A_0 S_0 \right) \right] \right) \right] \right) \right]. \end{aligned} \quad (51)$$

Fifth, rescale $g_1(S_0)$, $g_2(S_0)$:

$$\begin{aligned} \Phi_5(S_0) &\mapsto \Phi_6(S_0) \\ &= g_3(S_0) \left[d_2 + c_2 \tanh \left(b_2 + A_2 g_2(S_0) \left[d_1 + c_1 \tanh \left(b_1 + A_1 g_1(S_0) \left[d_0 + c_0 \tanh \left(b_0 + A_0 S_0 \right) \right] \right) \right] \right) \right]. \end{aligned} \quad (52)$$

Step 4: generalization to vector case

The above derivations take $S_0 \in \mathbb{R}$. For a spin system, S_0 is vector-valued. We generalize $\Phi_6(S_0)$, let $S_0 \in \mathbb{R}^N$, and transform scalar product to Hadamard product \odot , and let $b_k \in \mathbb{R}^N$, $d_k \in \mathbb{R}^N$, $A_k \in \mathbb{R}^{N \times N}$, $c_k \in \mathbb{R}^{N \times N}$, $k = 0, 1, 2$.

For $g_j(S_0)$, $j = 1, 2, 3$, we let $\gamma_j \in \mathbb{R}^{N \times N}$, $\beta_j \in \mathbb{R}^{N \times N}$, $\delta_j \in \mathbb{R}^N$, $\varphi_j \in \mathbb{R}^N$. Then

$$\Phi_6(S_0) = g_3(S_0) \odot \left[d_2 + c_2 \tanh \left(b_2 + A_2 g_2(S_0) \odot \left[d_1 + c_1 \tanh \left(b_1 + A_1 g_1(S_0) \odot \left[d_0 + c_0 \tanh \left(b_0 + A_0 S_0 \right) \right] \right) \right] \right) \right]. \quad (53)$$

The above $\Phi_6(S_0)$ is just the S_3 in Eq. (7). We need one more step to obtain the energy, i.e., summing up all components of $\Phi_6(S_0)$ to get a real scalar as the predicted energy.

IV. SYMMETRIZATION

In the main text, the symmetrization layer is given by

$$T_j(S_0) = \sum_{k=x,y,z} \text{conv}(S_{0,k}) \odot \text{conv}(S_{0,k}), \quad j = 0, 1, \dots, n. \quad (54)$$

We choose to use 2 different matrices as the filters for the 2 convolutional operations in $T_j(S_0)$, and rewrite $T_j(S_0)$ as

$$T_j(S_0) = \sum_{k=x,y,z} \text{conv}_{2j}(S_{0,k}) \odot \text{conv}_{2j+1}(S_{0,k}). \quad (55)$$

For conv_q , the convolution filter is $W_q \in \mathbb{R}^{C \times R \times S}$, C is the output channel number. The $[a, b, c]$ -th element of the convolution result is

$$\text{conv}_q(S_{0,k})[a, b, c] = \sum_{\alpha=0}^{R-1} \sum_{\beta=0}^{S-1} S_{0,k}[b + \alpha, c + \beta] W_q[a, \alpha, \beta], \quad (56)$$

where we assume a proper padding scheme is chosen in the above equation. Then

$$\text{conv}_{2j}[a, b, c] = \sum_{\alpha=0}^{R-1} \sum_{\beta=0}^{S-1} S_{0,k}[b + \alpha, c + \beta] W_{2j}[a, \alpha, \beta], \quad (57)$$

$$\text{conv}_{2j+1}[a, b, c] = \sum_{\gamma=0}^{R-1} \sum_{\delta=0}^{S-1} S_{0,k}[b + \gamma, c + \delta] W_{2j+1}[a, \gamma, \delta], \quad (58)$$

the $[a, b, c]$ -th element of the symmetrization layer reads

$$\begin{aligned} T_j(S_0)[a, b, c] &= \sum_{k=x,y,z} \text{conv}_{2j}(S_{0,k})[a, b, c] \cdot \text{conv}_{2j+1}(S_{0,k})[a, b, c] \\ &= \sum_{\alpha,\beta,\gamma,\delta} W_{2j}[a, \alpha, \beta] W_{2j+1}[a, \gamma, \delta] \sum_{k=x,y,z} S_{0,k}[b + \alpha, c + \beta] S_{0,k}[b + \gamma, c + \delta]. \end{aligned} \quad (59)$$

We let

$$s_1 = \begin{bmatrix} S_{0,x}[b + \alpha, c + \beta] \\ S_{0,y}[b + \alpha, c + \beta] \\ S_{0,z}[b + \alpha, c + \beta] \end{bmatrix}, \quad (60)$$

$$s_2 = \begin{bmatrix} S_{0,x}[b + \gamma, c + \delta] \\ S_{0,y}[b + \gamma, c + \delta] \\ S_{0,z}[b + \gamma, c + \delta] \end{bmatrix}. \quad (61)$$

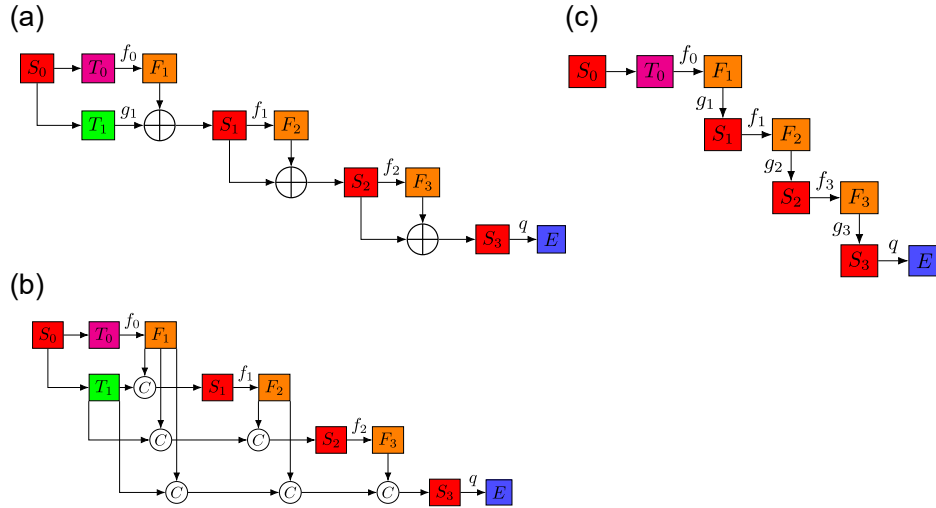


FIG. 3. (a) ResNet, (b) DenseNet, and (c) DNN adapted for Monte Carlo energy fitting of quantum double exchange model. \oplus is element-wise addition, while \textcircled{C} is concatenation.

Then

$$s_1^\top s_2 = \sum_{k=x,y,z} S_{0,k}[b + \alpha, c + \beta] S_{0,k}[b + \gamma, c + \delta]. \quad (62)$$

For a matrix $U \in O(3)$,

$$\begin{aligned} (Us_1)^\top Us_2 &= s_1^\top U^\top Us_2 \\ &= s_1^\top s_2. \end{aligned} \quad (63)$$

As a result, under any operation $U \in O(3)$, the value $T_j[a, b, c]$ remains invariant.

V. RESNET, DENSENET, DNN ADAPTED FOR MONTE CARLO ENERGY FITTING OF QUANTUM DOUBLE EXCHANGE MODEL

In this section, we present the structures of ResNet, DenseNet, and DNN, adapted for Monte Carlo energy fitting of quantum double exchange model.

As shown in Fig. 3(a) and Fig. 3(b), for ResNet and DenseNet, we add 2 symmetrization layers T_0 and T_1 to obtain $O(3)$ invariant results. For DNN in Fig. 3(c), we use 1 symmetrization layer T_0 , as no skip connection is used for DNN. How the nonlinear layers are computed, how the symmetrization is performed, and how the final energy is computed are similar to Fig. 3 in the main text.

VI. DQMC AND THE SPEED-UP BY EFNN

In this section, we explain the computational bottleneck problem in Determinant Quantum Monte Carlo (DQMC), and report the computational speed-up achieved by EFNN.

Outline of DQMC computation in 2D quantum double exchange model

For this quantum double exchange model, the DQMC computation has 3 major steps [7, 8].

1. Converting the Hamiltonian to quadratic form

The 2D quantum double exchange model is a lattice system describing electronic hopping interactions and on-site coupling between itinerant electrons and localized classical spins. In this framework, the classical spins act as a random field. The Hamiltonian reads (with chemical potential part)

$$H(S) = -t \sum_{\langle i,j \rangle, \alpha} (c_{i\alpha}^\dagger c_{j\alpha} + c_{j\alpha}^\dagger c_{i\alpha}) - \frac{J}{2} \sum_{i, \alpha, \beta} \vec{s}_i \cdot c_{i\alpha}^\dagger \vec{\sigma}_{\alpha\beta} c_{i\beta} - \mu \sum_{i\alpha} n_{i\alpha}, \quad (64)$$

$-t \in \mathbb{R}$ is the hopping amplitude, $-\frac{J}{2}$ is the on-site interaction strength, $\vec{s}_i \in \mathbb{S}^2$ is a classical spin vector. $\sigma^x, \sigma^y, \sigma^z$ are Pauli matrices. α, β denote spin components \uparrow and \downarrow .

We first need to expand the site index i to double index, the double index read $[a, b]$, $a, b = 0, 1, \dots, N-1$, denoting a lattice point on a square. Now a creation operator reads $c_{ab\uparrow}^\dagger$ or $c_{ab\downarrow}^\dagger$.

We group the creation operators into a row vector. The row vector has two parts,

$$c^\dagger = [c_{\uparrow}^\dagger, c_{\downarrow}^\dagger], \quad (65)$$

the first part c_{\uparrow}^\dagger is a row of creation operators with spin \uparrow , the explicit expression reads

$$c_{\uparrow}^\dagger = [c_{00\uparrow}^\dagger, c_{01\uparrow}^\dagger, \dots, c_{0,N-1,\uparrow}^\dagger, c_{10\uparrow}^\dagger, c_{11\uparrow}^\dagger, \dots, c_{1,N-1,\uparrow}^\dagger, \dots, c_{N-1,0,\uparrow}^\dagger, c_{N-1,1,\uparrow}^\dagger, \dots, c_{N-1,N-1,\uparrow}^\dagger]. \quad (66)$$

The creation operators in Eq. (66) are arranged in row-major order. Similarly, we arrange \downarrow creation operators in row-major order:

$$c_{\downarrow}^\dagger = [c_{00\downarrow}^\dagger, c_{01\downarrow}^\dagger, \dots, c_{0,N-1,\downarrow}^\dagger, c_{10\downarrow}^\dagger, c_{11\downarrow}^\dagger, \dots, c_{1,N-1,\downarrow}^\dagger, \dots, c_{N-1,0,\downarrow}^\dagger, c_{N-1,1,\downarrow}^\dagger, \dots, c_{N-1,N-1,\downarrow}^\dagger]. \quad (67)$$

The Hamiltonian in Eq. (64) is expressed in a quadratic form:

$$H(S) = c^\dagger \Gamma(S) c, \quad (68)$$

Hermitian matrix $\Gamma(S) \in \mathbb{C}^{2N^2 \times 2N^2}$,

$$\Gamma(S) = \begin{bmatrix} T_x + T_y & 0 \\ 0 & T_x + T_y \end{bmatrix} - \frac{J}{2} \begin{bmatrix} S^z & S^x - iS^y \\ S^x + iS^y & -S^z \end{bmatrix} + \begin{bmatrix} -\mu I & 0 \\ 0 & -\mu I \end{bmatrix}. \quad (69)$$

T_x and T_y are hopping matrices in x and y directions. For $T_x \in \mathbb{R}^{N^2 \times N^2}$, the $[rN + s, (r+1)N + s]$ -th element is $-t$, the $[(r+1)N + s, rN + s]$ -th element is $-t$, the rest are 0. The boundary condition is PBC, the r, s indices are understood as $r \bmod N, s \bmod N$. For hopping matrix $T_y \in \mathbb{R}^{N^2 \times N^2}$, the $[rN + s, rN + (s+1)]$ -th element and the $[rN + (s+1), rN + s]$ -th element are $-t$, the rest are 0. The boundary condition is PBC, the r, s indices are understood as $r \bmod N, s \bmod N$.

Matrix S^x contains all the s_{ab}^x components along the diagonal:

$$S^x = \text{diag}(s_{00}^x, s_{01}^x, \dots, s_{0,N-1}^x, s_{10}^x, s_{11}^x, \dots, s_{1,N-1}^x, \dots, s_{N-1,0}^x, s_{N-1,1}^x, \dots, s_{N-1,N-1}^x). \quad (70)$$

Matrix S^y contains all the s_{ab}^y components along the diagonal:

$$S^y = \text{diag}(s_{00}^y, s_{01}^y, \dots, s_{0,N-1}^y, s_{10}^y, s_{11}^y, \dots, s_{1,N-1}^y, \dots, s_{N-1,0}^y, s_{N-1,1}^y, \dots, s_{N-1,N-1}^y). \quad (71)$$

Matrix S^z contains all the s_{ab}^z components along the diagonal:

$$S^z = \text{diag}(s_{00}^z, s_{01}^z, \dots, s_{0,N-1}^z, s_{10}^z, s_{11}^z, \dots, s_{1,N-1}^z, \dots, s_{N-1,0}^z, s_{N-1,1}^z, \dots, s_{N-1,N-1}^z). \quad (72)$$

2. Convert tr to det

In this step, with the quadratic form in Eq. (68), the trace is converted to det, following the DQMC scheme:

$$\begin{aligned} Z(S) &= \sum_S \text{tr} e^{-\beta H(S)} \\ &= \sum_S \text{tr} e^{-\beta c^\dagger \Gamma(S) c} \\ &= \sum_S \det[I + e^{-\beta \Gamma(S)}]. \end{aligned} \quad (73)$$

In this step, the trace of a $4^{N^2} \times 4^{N^2}$ matrix is converted to the determinant of a $2N^2 \times 2N^2$ matrix, this is the quantum-to-classical mapping in DQMC.

More precisely, the partition function is

$$Z(S) = \int_{\{\bar{s}_{ab} \in \mathbb{S}^2: a, b=0,1,\dots,N-1\}} \text{tr} e^{-\beta H(S)} dS, \quad (74)$$

since all the classical continuous spins have norm 1. Eq. (73) can replace Eq. (74), only differing by a constant factor when the data points are dense and even enough.

3. Classical Monte Carlo using determinants

We use the determinants in Eq. (73) as statistical weight for Monte Carlo sampling. Determinants in Eq. (73) have the nice property that they are all strictly positive, because they can be written as

$$\det[I + e^{-\beta \Gamma(S)}] = \prod_{j=0}^{2N^2-1} [1 + e^{-\beta E_j(S)}] > 0, \quad (75)$$

$\{E_j(S)\}$ are the eigenvalues of Hermitian matrix $\Gamma(S)$. In each Monte Carlo step, we perform update on **one** component of **one** classical spin vector, among N^2 such 3D vectors in \mathbb{S}^2 . Evaluating Eq. (75) requires Exact Diagonalization (ED), for such $2N^2 \times 2N^2$ matrix, one evaluation requires complexity $O((2N^2)^3) = O(8N^6)$. Note that evaluating the det in left hand side of Eq. (75) has exactly the same complexity. There are $3N^2$ scalar components in S in total, a sweep to update every component has complexity $3N^2 \cdot O(8N^6) \sim O(24N^8)$. In order to obtain convergent results, we typically need 500 **effective samples**, then the total computational cost is

$$500 \times (\text{autocorrelation length}) \times (\text{sweep number}) \times O(24N^8). \quad (76)$$

As N increases, with computational complexity in Eq. (76), the computation becomes prohibitive for classical Monte Carlo very quickly. We use EFNN to address the computational bottleneck problem by training EFNN using exact value of Eq. (75), given S . We make one more transformation, and define a Monte Carlo energy $E_{\text{MC}}(S)$,

$$\begin{aligned} e^{-\beta E_{\text{MC}}(S)} &= \det[I + e^{-\beta \Gamma(S)}] \\ &= \prod_{j=0}^{2N^2-1} [1 + e^{-\beta E_j(S)}], \end{aligned} \quad (77)$$

then

$$E_{\text{MC}}(S) = -T \sum_{j=0}^{2N^2-1} \log[1 + e^{-\frac{1}{T} E_j(S)}]. \quad (78)$$

$E_{\text{MC}}(S)$ is formally a free energy. We use ED (Exact Diagonalization) to generate $[S, E_{\text{MC}}(S)]$ data as training set to EFNN. ED has the same complexity as determinant computation.

TABLE I. Average computational time for EFNN inference, $C = 3$, 3 layers, and ED, quantum double exchange model

N	10	15	20	25	30	35	40
EFNN time/s	4.56×10^{-3}	1.6×10^{-2}	1.62×10^{-2}	1.40×10^{-2}	7.08×10^{-3}	9.38×10^{-3}	7.59×10^{-3}
ED time/s	6.24×10^{-3}	3.11×10^{-2}	1.17×10^{-1}	4.82×10^{-1}	1.46	3.56	7.76

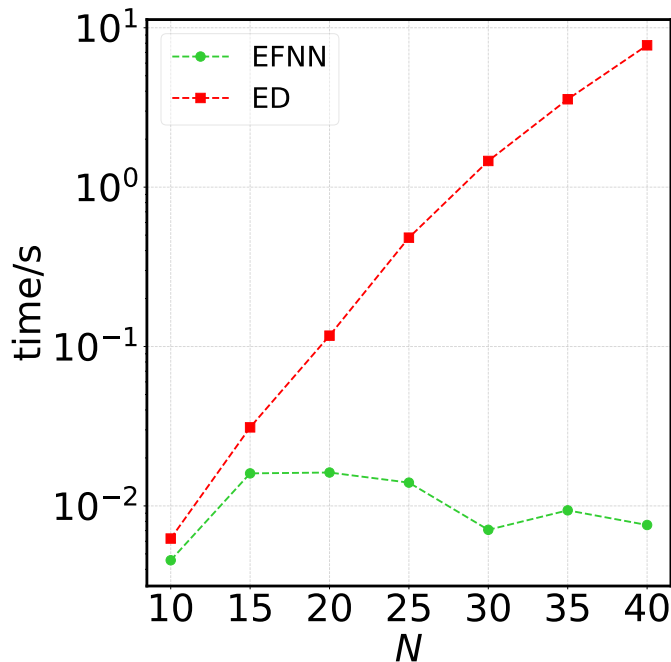


FIG. 4. Average computational time for EFNN inference, $C = 3$, 3 layers, and ED. The y-axis has log scale.

We report the average computation times of EFNN and ED in Table. I, and make a plot in Fig. 4, for comparison. While the EFNN model was trained on a supercomputer, this benchmark compares the inference time for a single $E_{\text{MC}}(S)$ value given a configuration S against the corresponding ED calculation, both performed on an Alienware m15 R12 laptop. As shown in Table. I and the green line in Fig. 4, the EFNN inference time remains approximately constant at order 10^{-2} s when the lattice size $N \times N$ grows from 10×10 to 40×40 . Conversely, as shown by the red line, the ED computational time scales polynomially with N , rapidly reaching approximately 10 s for $N = 40$. This scaling behavior makes ED computationally prohibitive for Monte Carlo sampling. Notably, for $N = 40$, the EFNN achieves a speedup of approximately 10^3 .

VII. DETAILS OF INFERENCE ERROR AND DATA DISTRIBUTION, QUANTUM DOUBLE EXCHANGE MODEL

In this section, we report the error of EFNN prediction, plot the distributions of the test data (ground truth) and the EFNN predictions, for the quantum double exchange model.

We report the absolute value of mean of E_{MC} for test set, RMSE of prediction by EFNN, and relative error in Table. II, with $C = 3$, layer number = 3, in quantum double exchange model. The relative error is defined as

$$\frac{\text{RMSE}}{|\text{mean of } E_{\text{MC}}|}. \quad (79)$$

As shown in Table. II, even though the model is trained on a 10×10 lattice under boundary condition PBC, when applied to larger lattices, the RMSE increases only marginally. Moreover, the $|\text{mean of } E_{\text{MC}}|$ increases very quickly with respect to N . As a result, the difference of the prediction value by EFNN and the ground truth value of $E_{\text{MC}}(S)$, becomes smaller and smaller perturbations as N increases, demonstrating the accuracy of EFNN.

We present the histograms of test set data (Y_{test} , ground truth value of $E_{\text{MC}}(S)$) and prediction results computed by EFNN (Y_{pred} , predicted value of $E_{\text{MC}}(S)$) for the quantum double exchange model in Fig. 5, for $N = 10, 15, 20, 25, 30, 35, 40$. The blue histograms are for ground truth data Y_{test} , and green histograms are for predictions Y_{pred} . Note that as lattice size increases, the model trained on 10×10 lattice still correctly predicts $E_{\text{MC}}(S)$ for larger lattices, up to $N = 40$, as shown by the overall histogram shapes, and the mean values of Y_{test} and Y_{pred} . Note that as N increases, the absolute value of mean Y_{test} increases.

TABLE II. Performance metrics for EFNN, $C = 3$, 3 layers, quantum double exchange model

N	10	15	20	25	30	35	40
$ \text{mean of } E_{\text{MC}} $	51.6508	116.1850	206.5729	322.7573	464.7841	632.5962	826.2887
RMSE	0.0584	0.0989	0.1340	0.1714	0.2118	0.2549	0.3003
relative error	1.13×10^{-3}	8.51×10^{-4}	6.49×10^{-4}	5.31×10^{-4}	4.56×10^{-4}	4.03×10^{-4}	3.63×10^{-4}

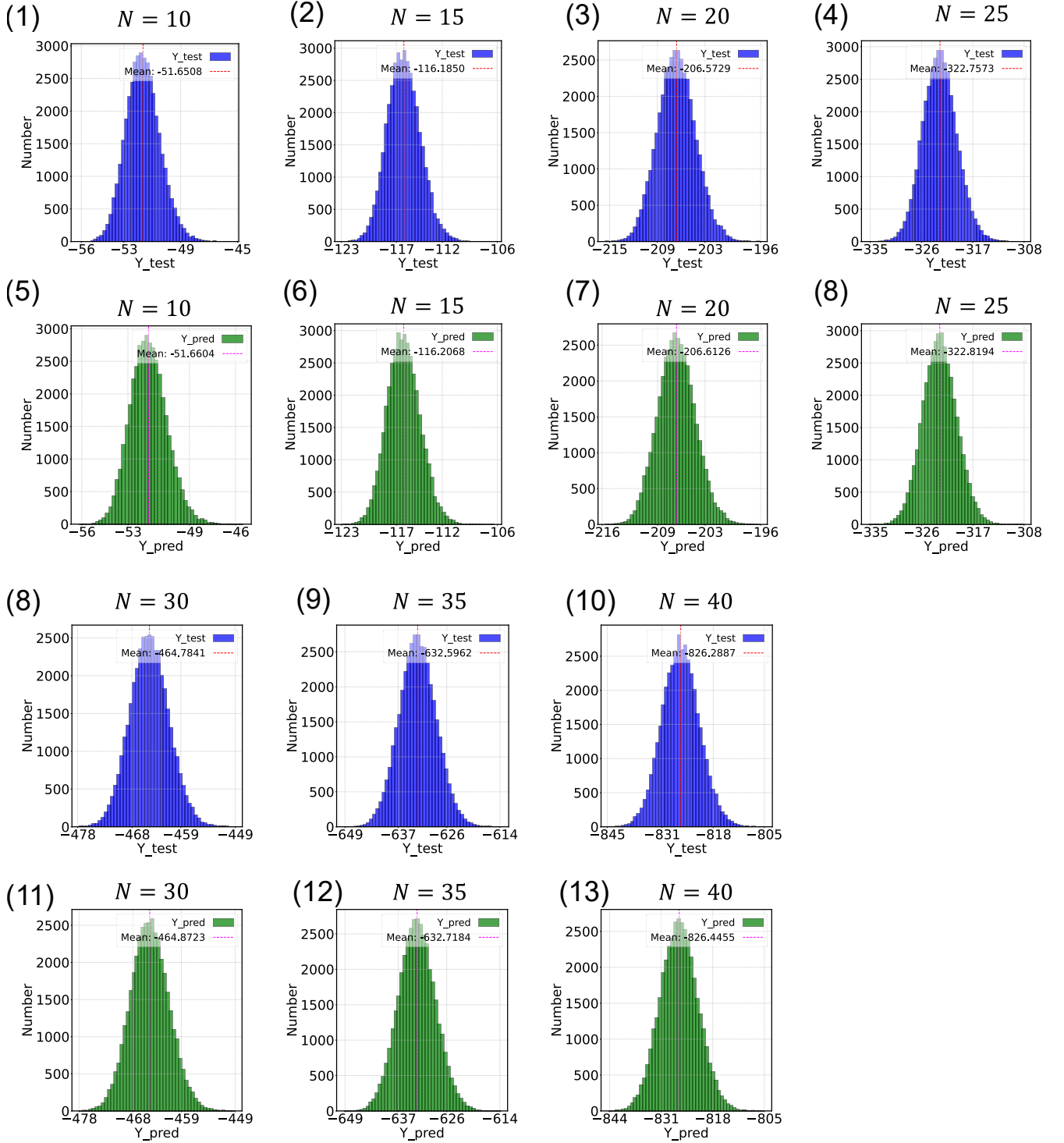


FIG. 5. EFNN's prediction results of quantum double exchange model, with $C = 3$ and 3 layers: histogram of Y_{test} and Y_{pred} , for $N = 10, 15, 20, 25, 30, 35, 40$.

-
- [1] A. H. Al-Mohy and N. J. Higham, A New Scaling and Squaring Algorithm for the Matrix Exponential, *SIAM Journal on Matrix Analysis and Applications* **31**, 970 (2010).
 - [2] C. M. Bender and S. A. Orszag, *Advanced Mathematical Methods for Scientists and Engineers I*, 1st ed. (Springer New York, New York, NY, 1999).
 - [3] V. Yukalov and E. Yukalova, Higher Orders of Self-Similar Approximations for Thermodynamic Potentials, *Physica A: Statistical Mechanics and its Applications* **206**, 553 (1994).
 - [4] V. Yukalov and S. Gluzman, Self-Similar Bootstrap of Divergent Series, *Physical Review E* **55**, 6552 (1997).
 - [5] V. Yukalov and S. Gluzman, Self-Similar Exponential Approximants, *Physical Review E* **58**, 1359 (1998).
 - [6] V. Yukalov and E. Yukalova, Self-Similar Structures and Fractal Transforms in Approximation Theory, *Chaos, Solitons & Fractals* **14**, 839 (2002).
 - [7] Z. Bai, Lecture notes on determinant quantum monte carlo (dqmc), University of California, Davis, Department of Computer Science (2009), accessed: 2023-10-27.
 - [8] E. LOH and J. GUBERNATIS, Chapter 4 - stable numerical simulations of models of interacting electrons in condensed-matter physics, in *Electronic Phase Transitions*, Modern Problems in Condensed Matter Sciences, Vol. 32, edited by W. HANKE and Y. KOPAEV (Elsevier, 1992) pp. 177–235.